Journal of Science: Advanced Materials and Devices 8 (2023) 100527

Contents lists available at ScienceDirect

Journal of Science: Advanced Materials and Devices

journal homepage: www.elsevier.com/locate/jsamd

Original Article

Solar energy harvesting using lead-free pyroelectric bulk ceramics: A simulation study

Nishchay Saurabh [a], Raj Kiran [b], Satyanarayan Patel [a, *]

[a] Department of Mechanical Engineering, Indian Institute of Technology Indore, Madhya Pradesh, 453 552, India
[b] School of Mechanical and Aerospace Engineering, Nanyang Technological University, 50 Nanyang Avenue, 639798, Singapore

ARTICLE INFO

Article history:
Received 9 September 2022
Received in revised form
22 November 2022
Accepted 29 November 2022
Available online 5 December 2022

Keywords:
Pyroelectric
Solar energy harvesting
Power-boosting circuit
Lead-free ceramic
P–SSHI and H–SSHI

ABSTRACT

Solar radiation and wind provide the temporal temperature fluctuation for heating and cooling. 0.005La–$Na_{0.5}Ba_{0.5}TiO_3$-0.06$BaTiO_3$-0.002Ta is found as the best suitable material for energy harvesting. The voltage and power output are further improved by tuning operating frequency, load capacitance and resistance. Maximum power of 6.7 μW is obtained at a frequency of 0.04 Hz, load capacitance of 1 μF and resistance of 25 MΩ. A nonlinear electrical circuit based on parallel synchronized switched harvesting on the inductor (P–SSHI) and hybrid synchronized switched harvesting on the inductor (H–SSHI) are used to enhance the power. The power is increased by 54% and 34.6% under P–SSHI and H–SSHI, respectively. However, H–SSHI was preferred for power-boosting because of the self-triggering process and low energy losses. This work shows the potential of lead-free pyroelectric materials for solar energy harvesting with losses in the circuit.

1. Introduction

The growing energy demand has forced researchers to move towards self-powered, clean and renewable energy sources. In this regard, solar, wind and tidal energies are considered the most prominent renewable energy sources. Solar energy has already been used for photovoltaic cells [1], thermoelectric generators [2] and thermal power plants [3] to harness energy. However, in this context, the heat energy obtained from the solar can be an abundant and omnipresent energy source. Thus, pyroelectric materials that convert temperature fluctuations into electrical energy can also be employed for solar energy harvesting [4–7]. Materials with high pyroelectric coefficients at room temperature and low dielectric loss are suitable for solar energy harvesting. Lead-free pyroelectric materials such as (1-x) $Na_{0.5}Ba_{0.5}TiO_3$-x$BaTiO_3$ [8,9], $Ba_{0.85}Ca_{0.15}Zr_{0.1}Ti_{0.9}O_3$ [10,11], $K_{0.5}Na_{0.5}NbO_3$ [12] are used due to their high pyroelectric coefficient, superior figures of merit (FOM) and energy storage capabilities. Several FOMs are defined for pyroelectric material depending on the thermal and electrical circuit considered. The pyroelectric performance of the materials is assessed using these FOMs to maximize current or voltage for specific power input applications like thermal imaging sensors. In this regard, the voltage responsivity and current responsivity of pyroelectric FOMs are defined as $F_v = \frac{p}{c_v \epsilon_r \epsilon_0}$ and $F_i = \frac{p}{c_v}$ [13], respectively, where p is a pyroelectric coefficient, c_v is volume-specific heat, ϵ_0 is the permittivity of free space, ϵ_r dielectric constant and tan δ is the dielectric loss. The pyroelectric FOM for infrared detection is expressed as $F_C = \frac{p}{\sqrt{\epsilon_r}}$, energy harvesting FOM is $F_e = \frac{p^2}{\epsilon_r \epsilon_0}$ and high detectivity-based FOM is $F_d = \frac{p}{c_v \sqrt{\epsilon_r \epsilon_0 \tan \delta}}$ [8,14,15]. The selection of pyroelectric materials under a definite heat can be made based on the modified FOM $F_e^* = \frac{p^2}{\epsilon_r \epsilon_0 c_v^2}$, developed by Zebek et al. [15].

In this regard, Balakat et al. [16] utilized 0.005La–$Na_{0.5}Ba_{0.5}TiO_3$-0.06$BaTiO_3$-0.002Ta and obtained a pyroelectric coefficient (p) of 12.9×10^{-4} C m^{-2} K^{-1} and dielectric constant of 671. The FOM for energy harvesting is comparable with commercial $PbZr_xTi_{1-x}O_3$. Further, $(Ba_{0.84}Ca_{0.15}Sr_{0.01})(Ti_{0.90}Zr_{0.09}Sn_{0.01})O_3$ consists of an excellent p of 11.16×10^{-4} C m^{-2} K^{-1} and is considered for the frequency independent (100–2000 Hz) pyroelectric FOMs [17]. Moreover, Sharma et al. [11] have shown that $Ba_{0.85}Ca_{0.15}Zr_{0.1}Ti_{0.9}O_3$ has a higher p of 8.6×10^{-4} C m^{-2} K^{-1} with a dielectric constant of 3125 can also be used for pyroelectric energy harvesting. Further, water and air were used by Sharma et al. [18] as two different cooling mediums to provide rapid temperature fluctuations. However, a continuous temperature gradient is a limitation of using these pyroelectric materials. Therefore, Krishnan et al. [19] considered a wind turbine-based chopper disc with speed-reduction gears to modulate the solar radiation falling on the surface, leading to a

* Corresponding author.
E-mail addresses: phd2001203003@iiti.ac.in (N. Saurabh), me123025@mnnit.ac.in (R. Kiran), spatel@iiti.ac.in (S. Patel).

Peer review under responsibility of Vietnam National University, Hanoi.

https://doi.org/10.1016/j.jsamd.2022.100527

temperature gradient. In this direction, a three-dimensional pattern was implemented to enhance temporal fluctuations rates by inducing lateral temperature gradients on the sidewall of the responsive material [20]. These methods provide a basis for successfully incorporating pyroelectric materials-based solar energy harvesting systems.

In this direction, researchers have deployed various methods for energy harvesting using pyroelectric materials. Nguyen et al. [21] used a Teflon chamber with a cylinder oscillating between hot and cold sources using poly (vinylidene fluoride–trifluoroethylene)(P(VDF-TrFE) to generate energy. The maximum energy density generated was 130 kJ m^{-3} at 0.061 Hz within a temperature range of 342–360 K and electric field (0.2–0.74 MV m^{-1}). The pyroelectric energy harvester also shows great potential for practical industrial application. Hybrid pyroelectric energy harvesters can be used in various fields to increase the energy conversion potential. In this direction, Lee et al. [22] used a nanogenerator consisting of piezo-pyroelectric micro-patterned polyvinylidene fluoride polytrifluoroethylene with graphene nanosheets (to increase thermal conductivity) and carbon nanotubes (to increase flexibility). This was used to harvest temperature differences as well as mechanical stress. Further, pyroelectric harvesters are used for exhaust gas heat recovery [23], water splitting for hydrogen generation [24], oscillating heat pipe [25] and wind-driven [26] energy harvesters. The polymer-based pyroelectric device has a huge potential for wearable and implantable devices in the human body. Further, Lee et al. [27] employed the Olsen cycle to convert waste heat into electrical energy and P(VDF-TrFE) was placed alternatively with a hot and cold source. Thus, generated energy was 155 kJ m^{-3} at 0.066 Hz in the temperature range (298–383 K) and electric field (0.2–0.35 MV m^{-1}). Though the energy obtained was not very high, these were the initial steps in pyroelectric energy harvesting. Later, Caudaras et al. [28], applied heating and cooling cycles to generate a current of 0.1 μA, using temperature fluctuation in the 300–360 K range. The current obtained was rectified and stored in the capacitor of 1 μF. Zhang et al. [29] incorporated solar micro-energy and wind flow for pyroelectric energy harvesting in PZT; temperature variation and power density were obtained as 0.53 K/sec and 4.2 W m^{-3}. Later, Sharma et al. [30] used different types of pyroelectric materials to compute solar energy harvesting analytically. The maximum voltage, power generated and stored energy were 11.47 V, 4.9 μW and 576 μW, respectively, for $Sr_{0.5}Ba_{0.5}Nb_2O_6$ across the load capacitance of 4.7 μW. However, Sharma et al. [30] assumed that the pyroelectric current present in the circuit is rectified, resulting in overestimating the voltage and power. Several power-enhancing circuits [31–34] have been employed in the case of piezoelectric material to scavenge the vibrational/mechanical energy into electrical energy [35–37]; in contrast, little work has been done for the pyroelectric material [5,38]. Various researchers proposed and used solar energy harvesting using pyroelectric materials in this regard. However, they did not focus on the high pyroelectric coefficient-based lead-free material selection and execution of different electric circuits. Thus, this work considers lead-free pyroelectric material with a high pyroelectric coefficient and a low dielectric constant in 293–335 K. The temperature range was chosen based on the maximum temperature of the material that can be reached by solar heating.

The work's novelty lies in the electrical circuits' modeling to mimic the losses with real-world conditions and the adaptation of power-boosting circuits to enhance the pyroelectric solar energy harvesting capabilities. The paper's main goal was to ascertain whether the energy harvested could be stored or used to create a self-harvesting system. This work shows pyroelectric-based solar energy harvesting with power-boosting circuits for self-powering sensors and devices. The organization of the work is to proceed with the finding of temperature and the corresponding current profile from the solar radiation for the pyroelectric materials. The most efficient material is chosen from the output voltage obtained after the variation in load capacitance. Further, the voltage and power are calculated based on the most efficient load resistance and frequency. Finally, power-boosting circuits such as parallel synchronized switch harvesting on an inductor (P–SSHI) and hybrid synchronized switch harvesting on an inductor (H–SSHI) are employed to enhance power output.

2. Materials and methodology

Initially, a heating and cooling cycle is used, incorporating materials properties, then converting the obtained temperature cycle into the pyroelectric current. The obtained solar energy-based pyroelectric current will be harvested with different electrical circuits. Figs. 1 and 2 depict the schematic of solar energy harvesting through pyroelectric material using a full-wave rectifier (FWR) circuit, parallel synchronized switch harvesting on an inductor (P–SSHI) and hybrid synchronized switch harvesting on an inductor (H–SSHI), respectively.

The entire process of solar energy harvesting can be divided into three sections: (a) temperature fluctuations, (b) electrical equivalent circuit of pyroelectric material, and (c) power electronics to utilize or store energy, as shown in Figs. 1 and 2. The heating of pyroelectric material was brought by solar radiation falling on the material's surface. The mean solar radiation (700 W m^{-2}) is considered as heat source [30]. Natural convection and solar radiation losses were also taken in this heating process. The material was shielded from sunlight and forced convective air in the form of environmental wind flow was used to cool the material. However, an external source of forced convection is required at a higher frequency to cool material due to a short time interval. A similar modulation mechanism consisting of a chopper disk and speed-reduction gears powered by wind energy has already been used [19]. It is challenging to incorporate the thermal variation available in the environment, as the random fluctuations in the environment cannot be simulated with fixed boundary conditions. However, the thermal parameters under consideration were taken to be the lower side of the fluctuations. In this regard, Caudaras et al. [28] showed that the difference in thermal variation under environmental conditions and laboratory can be balanced with the increases in the volume of the pyroelectric material. Hence, the volume of material under consideration was similar to the work done by Caudaras et al. [28] to incorporate environmental fluctuations. The pyroelectric material's thickness (b_m) and surface area (A_m) were taken as 1×10^{-4} m and 5×10^{-4} m^2, respectively. The samples' top and bottom surfaces are assumed to be silver electrodes for charge conduction. Norkus et al. [39] study shows that a surface painted with a silver black coating not only acts as an electrode but also enhances α (absorptivity) to be greater than 0.93. Further, as the entire study was conducted at the thermal equilibrium condition, the e (emissivity) of the material can also be assumed to be increased. Further, Sharma et al. [30] work has assumed the α and e as 0.8; thus, the same has been adopted in the present work. The temperature fluctuations solar heating provides on pyroelectric materials generate electric potential and result in current/voltage flow when a circuit is connected at the two ends. This leads to the second section of the system, where pyroelectric material represents an electrical source; see Figs. 1 and 2. The electric circuit consists of a current source, material resistance (R_m) and capacitance (C_m) connected in parallel as equivalent pyroelectric material [28]. The last part (as depicted in Figs. 1 and 2) would deal with different power circuits, P–SSHI and H–SSHI to boost and rectify the obtained voltage from the pyroelectric material. The P–SSHI and H–SSHI are used with FWR in the present analysis.

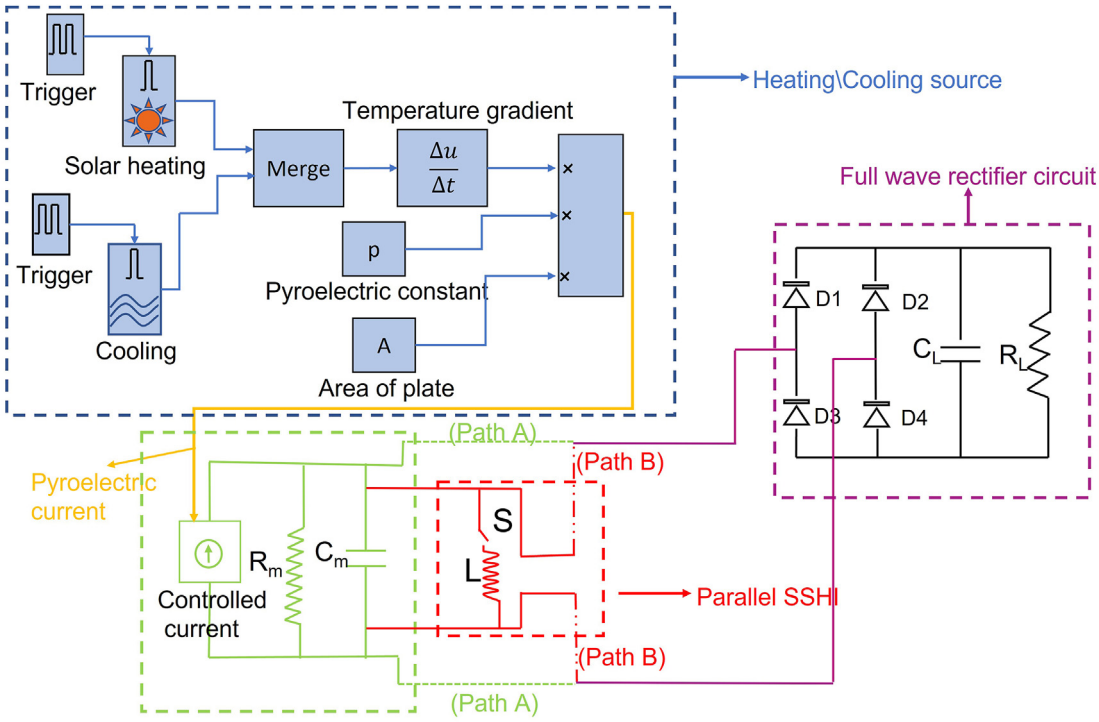

Fig. 1. Schematic of the solar energy harvesting based electrical equivalent circuit of pyroelectric material for full-wave rectifier circuit (FWR) path A and parallel synchronized switch harvesting on inductor (P−SSHI) with FWR path B.

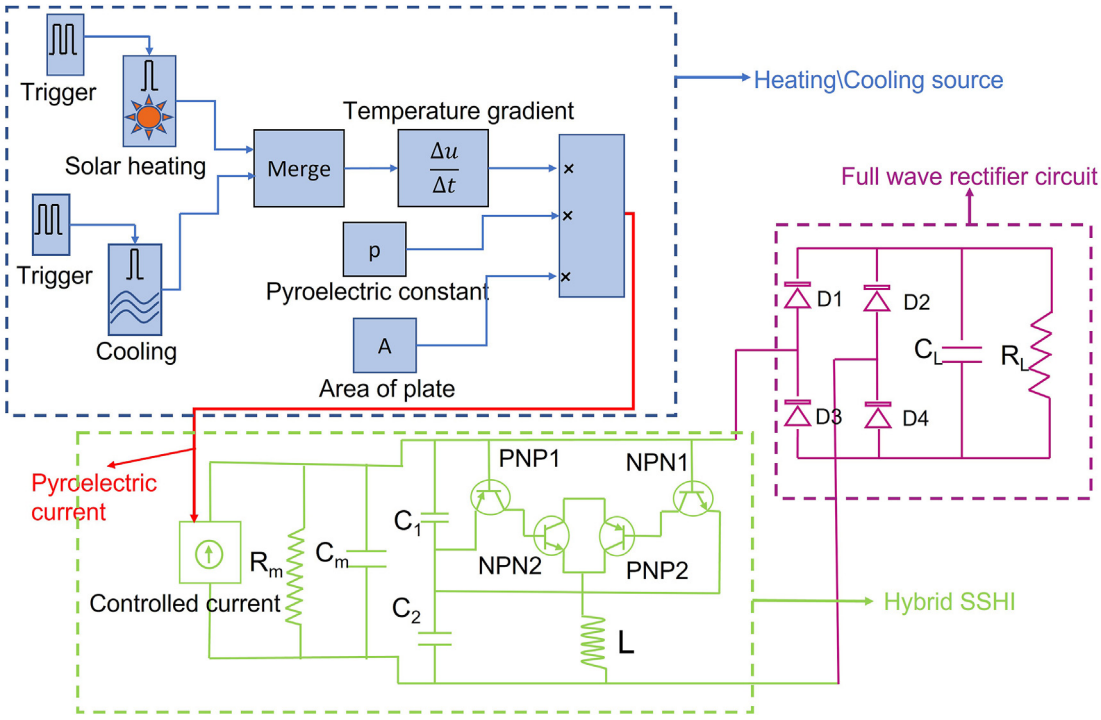

Fig. 2. Schematic of the solar energy harvesting based electrical equivalent circuit of pyroelectric material for hybrid synchronized switch harvesting on inductor (H−SSHI) circuit with full-wave rectifier circuit (FWR).

In the present work, the temperature fluctuations are kept in the temperature range of 293−335 K for energy harvesting. The pyroelectric properties used for the present work are specific heat capacity (H_m), density, thermal conductivity (k_m), pyroelectric coefficient (p), dielectric constant (ε), volume resistivity and Curie temperature provided in Table 1. The materials chosen for the present analysis include $0.005La-Na_{0.5}Ba_{0.5}TiO_3$-$0.06BaTiO_3$-0.002Ta (La-NBT-BT-Ta) [16], $(Ba_{0.84}Ca_{0.15}Sr_{0.01})(Ti_{0.90}Zr_{0.09}Sn_{0.01})O_3$ (BCSTZS) [17], $Ba_{0.85}Ca_{0.15}Zr_{0.1}Ti_{0.9}O_3$ (BCZT) [11,40,41], $0.98(0.98Bi_{0.5}Na_{0.5}TiO_3$-$0.02BiAlO_3)$-$0.02(Na_{0.5}K_{0.5})NbO_3$ (BNT-BA-

Table 1
Lead-free pyroelectric materials properties were used for analysis.

Materials		La-NBT-BT-Ta [16]	BCSTZS [17]	BCZT [11,40,41]	BNT-BA-0.02KNN [42,43]	KNN [44–46]	SBN [30]
Specific heat capacity	$x10^6$ JK^{-1} m^{-3}	2.8	2.33	2.11	2.8	2.47	2.34
Thermal conductivity	W m K^{-1}	3	2.2	2.2	3	2.4	1.1
Pyroelectric coefficient	$x10^{-4}$ C m^{-2} K^{-1}	12.92	11.16	8.6	8.04	3.38	5.5
Dielectric constant	–	671	3500	3125	880	2017	2000
Volume resistivity	x 10^9 Ω m	1.32	5.60	5.60	0.305	2.00	2.00
Density	kg m^{-3}	5800	5400	4600	5840	4500	4982
Curie temp	C	61.3	80	83	80	340	70

0.02KNN) [42,43], 0.96 ($K_{0.5}Na_{0.5}NbO_3$)-0.04$Bi_{0.5}Na_{0.5}ZrO_3$ (KNN) [44–46] and SBN [30], see Table 1. These materials are selected based on their p (high p provides a higher pyroelectric current) and ε (lower ε reduces the material capacitance) from the latest literature. The previous results [30,47] show SBN to be best performing lead-free material than popular pyroelectric materials such as TGS (Triglycine sulphate), $LiTaO_3$ and PMN-PT($68PbMg_{1/3}Nb_{2/3}O_3$–$32PbTiO_3$) crystals. Thus, SBN is considered along with other lead-free pyroelectric materials in the preset work. It should be noted that the present work considers $BaTiO_3$, $Na_{0.5}Ba_{0.5}TiO_3$ and $K_{0.5}Na_{0.5}NbO_3$-based composition with maximum p. These lead-free families are well known and explored for their pyroelectric application point of view.

3. Model analysis

The temperature fluctuation (heating of pyroelectric material) provided by solar radiation can be given as [19,30],

$$H_m \times Vol_m \times \frac{dT}{dt} = Q_{pyro} - Q_{conv} - Q_{rad} \tag{1}$$

where Vol_m is the volume of the material, $\frac{dT}{dt}$ is the temperature gradient with time. $Q_{pyro} = \alpha \times A_m \times W_{solar}$ is the thermal energy falling on the surface of the pyroelectric material due to solar radiation, where α is the absorptivity of the material and W_{solar} is solar radiation falling on the material's surface (taken as 700 W/m^2). $Q_{conv} = \frac{T_i - T_0}{r_{cond} + r_{conv}}$ is the effect of natural convection and conduction losses arising from the surface of the pyroelectric material, T_i is the instantaneous material temperature and T_0 is the ambient temperature, $r_{cond} = \frac{b_m}{k_m A_m}$ and $r_{conv} = \frac{1}{h_a A_m}$ where h_a is the convective heat transfer coefficient of the air. $Q_{rad} = e \times \sigma \times A_m \times (T_i^4 - T_0^4)$ is the energy loss due to thermal radiation as all body radiates at all temperatures, where e is the material's emissivity, $\sigma = 5.87 \times 10^{-8}$ W m^{-2} K^{-4}. Thus, Q_{conv} and Q_{rad} are the losses considered during the heating cycle. The lumped heat transfer with a Biot number lesser than 0.1 was assumed to obtain the transient temperature profile. The cooling is obtained by preventing solar radiation from falling on the surface using a disc and environmental wind/airflow. It is assumed that the wind flows at 2–4 m s^{-1}. The disc can also be operated using wind energy and synchronized with speed-reduction gears for the heating/cooling cycle. The cooling of the material can be given as

$$H_m \times Vol_m \times \frac{dT}{dt} = -Q_{Fconv} - Q_{rad} \tag{2}$$

where Q_{Fconv} is the heat loss due to the forced convection and expression is the same as discussed for the heating cycle. The wind velocity is applied for forced heat convection. In the heating cycle, the material is heated from room temperature to T and the cooling cycle cools the material from T to room temperature, as shown in Fig. 3(a). The temperature profile attained from heating and cooling cycle was used to obtain a temperature gradient. It was further employed to calculate pyroelectric current (I_p) by [48]

$$I_p = A_m \times p \times \left(\frac{dT}{dt}\right) \tag{3}$$

where $\left(\frac{dT}{dt}\right)$ is the temperature gradient obtained from the heating–cooling cycle. The pyroelectric current (I_p) is used as a source for the equivalent electric circuit, as shown in Figs. 1 and 2. The equivalent pyroelectric circuit consists of low capacitance and high resistance (obtained from material dielectric loss and volume resistivity) combined with the source current. The I_p obtained for all the materials considered in the present work is depicted in Fig. 3(b).

The I_p and voltage generation can be extracted using an external circuit. However, the current/voltage would be alternating due to the alternative heating/cooling cycle. Hence, to obtain a unidirectional flow, it is essential to use an FWR (see Fig. 1 path A). The diodes D1 and D3 allowed the flow of charges in the heating cycle, whereas diodes D2 and D4 restricted the reverse flow of charges. Though diodes D2 and D4 allowed the current flow during the cooling cycle, D1 and D4 restricted the backward flow of current, as shown in Fig. 1 path A. Further, a load capacitor (C_L) is used to store the charge and the voltage after the nth cycle in C_L can be given as [28,30].

$$V(n) = \frac{Q}{C_m + C_L} + V(n-1)\frac{C_L - C_m}{C_L + C_m} \tag{4}$$

where Q is the charge stored after rectification in one cycle. Moreover, the voltage across the load resistor (R_L) connected in parallel with the material can be found using Kirchhoff's equation for the FWR (Fig. 1 path A) as [30],

$$C\frac{dV_o}{dt} + \frac{V_o}{R} = I_P \tag{5}$$

where $C = C_m + C_L$ and $\frac{1}{R} = \frac{1}{R_m} + \frac{1}{R_L}$, the voltage ($V_o$) is measured across R_m. Since the losses around the diodes are considered, the voltage across the pyroelectric material (V_m) can be given as

$$V_m = V_o + 2{*}V_d \tag{6}$$

Fig. 1 (path A) shows the standard FWR circuit connected with a capacitor (C_L) to smooth current flow through R_L. The efficiency of the power output from the FWR circuit is similar to that obtained from directly connecting the load resistor across the pyroelectric material. However, this arrangement can help store the charge for later use. In order to enhance power, a nonlinear switched charge extraction approach is used, which is extensively employed for piezoelectric energy harvesting [31–34]. Thus, similar circuits are also considered in the present work. Fig. 1 (path B) and Fig. 2 show the nonlinear switch energy harvesting based on P–SSHI and H–SSHI circuits, respectively. Further, in the case of P–SSHI, I_p and

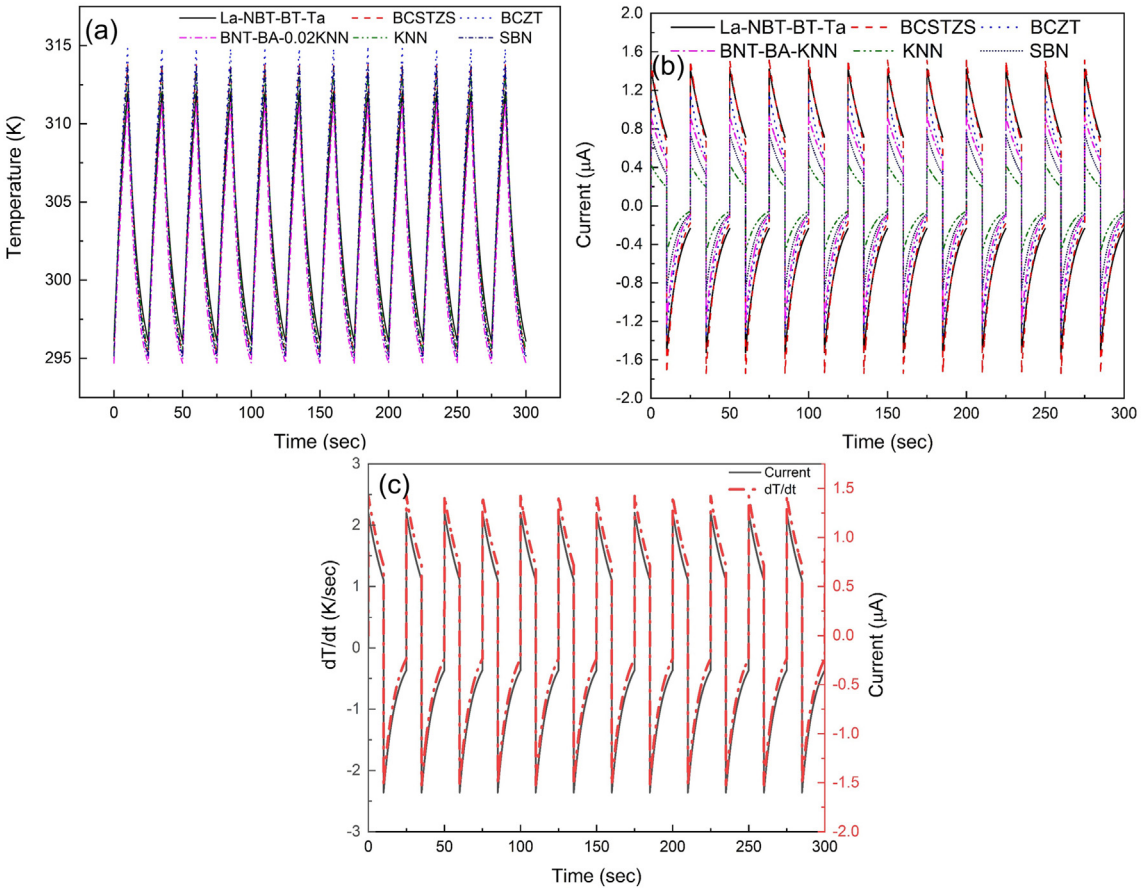

Fig. 3. (a) Temperature as a function of time profile and (b) Current versus time plots for all the pyroelectric materials and (c) Variation of temperature gradient (dT/dt) with time and current for La-NBT-BT-Ta.

voltage across the pyroelectric material (V_m), when the switch is on, can be expressed as (see Fig. 1(a) path B) [49],

$$I_p = C_m \frac{dV_m}{d_t} + i_L + \frac{V_m}{R_L} \tag{7}$$

where

$$V_m = L\frac{di_L}{dt} \tag{8}$$

where L is the inductance and i_L current flows through the inductor. The P−SSHI works on the principle that L and C_m form parallel tuned circuits when the switch is turned on. The time of the trigger is defined by [5]

$$t = \pi\sqrt{LC_m} \tag{9}$$

Thus, the discharge through the inductor L leads to inversion and enhancement of V_o. Though, due to the losses in the electric circuit, the inversion is not perfect. Fig. 2 presents H−SSHI [50], where the heating/cooling and rectification remain the same as the FWR and P−SSHI. However, the H−SSHI circuit has two additional capacitors (C_1 and C_2) compared to P−SSHI, which are employed to detect the negative and positive peaks applied for self-switching. The electric circuits' properties are defined in Table 2, such as the voltage drop across the diode, inductance (L) and capacitance used. Further, H−SSHI consists of transistors, as shown in Fig. 2; the

Table 2
Electrical properties of the circuits [50].

Properties	FWR	P−SSHI	H−SSHI
Diode drop	0.53 V	0.53 V	0.53 V
L	–	10 μH	5 μH
C1	–	–	10 pF
C2	–	–	1 nF

advantage of using them is that it requires low power and less switching time [50]. NPN and PNP transistors along with capacitors (*C1* and *C2*) are employed. The H−SSHI makes the switching process automatic, using power from the circuit and reducing the dependency on external triggering. The rest of H−SSHI circuit working remains identical to P−SSHI. The entire process of voltage amplification can be divided into four modes for H−SSHI. In the first mode, $V_m = V_o + 2V_d$, where V_m is the voltage across the C_m, V_o is the voltage across the load resistor (R_L) and V_d is the voltage drop across the diode. Hence, the voltage across *C1* is positive, making transistors PNP1 and NPN2 off as PNP1 requires negative voltage to switch on. Further, NPN1 is turned on but unable to switch on PNP2 due to positive voltage requirements. As a result, all transistors would be turned off, causing the circuit to behave like an FWR. The second mode $V_m < V_o + 2V_d$ is the period of voltage flipping from positive to negative. Here, diodes in FWR will be off due to the low voltage. However, slowly changing the voltage across *C1* from positive to negative. This reversal turns on PNP1 as soon as V_{base} (voltage required to conduct transistor) is achieved and further

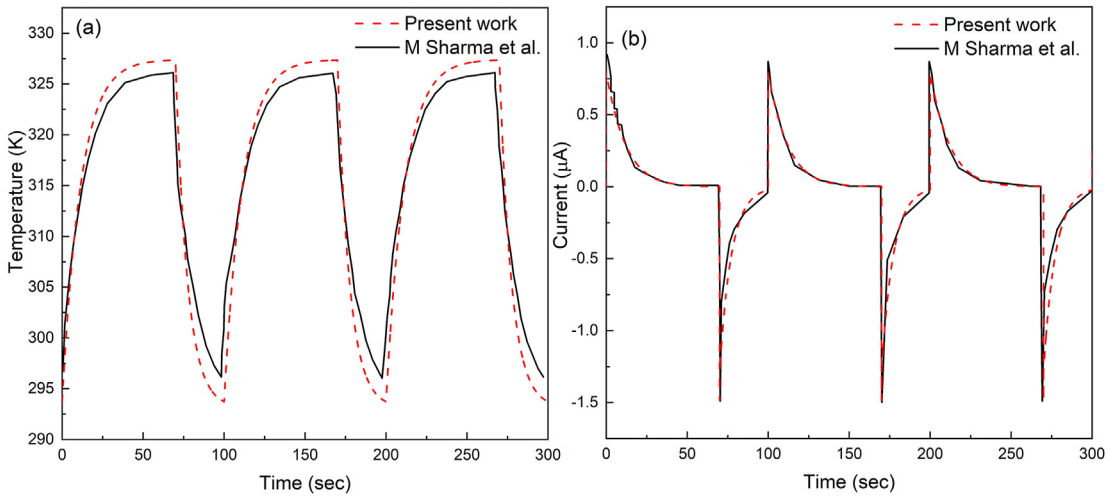

Fig. 4. Variation of (a) temperature and (b) current with time for SBN at 0.01 Hz for present work and Sharma et al. [15].

turns on NPN2. I_p will flow through the LC circuit and voltage flipping occurs due to the current reversal (onset cooling cycle). This process occurs until the current flowing through the inductor becomes zero or the voltage flipping has been done. Consequently, turning off the PNP1 and NPN2 transistors and taking the circuit to the initial position where no diode is conducting and all transistors are off. Therefore, building the flipped voltage to - (V_o+2V_d). In modes 3 and 4, operations would be similar to modes 1 and 2; only the current flow through the inductor would be reversed because of the voltage flip from - (V_o+2V_d) to (V_o+2V_d). The equations (1)–(9) were used to solve the heating/cooling temperature profile, current profile and power circuits using MATLAB's SIMULINK/SIMSCAPE model.

4. Results and discussions

Initially, the heating/cooling cycle was considered at 0.04 Hz, where pyroelectric material was heated 40% of the time and cooled 60% of the time, as shown in Fig. 3(a). The heating and cooling cycle duration was obtained considering solar radiation and forced convection by the wind as fixed parameters, respectively. The maximum increase in temperature was observed for BCZT as 314.8 K. However, a significant temperature variation was not found in all pyroelectric materials, as seen in Fig. 3(a). This is due to the material's thermal heat capacity, which remains almost the same for all materials used in this study.

Further, the time derivative temperature profile was employed to obtain current and the results are shown in Fig. 3(b). The maximum current of 1.74 μA was found for BCSTZS, whereas La-NBT-BT-Ta consists of the maximum p as given in Table 1. Though the specific heat capacity effect is not much for the maximum temperature attained, this may affect the heat transfer process and decrease the dT/dt as in the case of the La-NBT-BT-Ta (H_c = 2.8) and BCSTZS (H_c = 2.33). Fig. 3 (b) shows a sharp increase in the current due to a rapid decrease in surface charges at ambient temperature under the applied heat flux. If the temperature gradient is dT/dt > 0, the level of spontaneous polarization decreases as the orientation of the dipoles within the material is lost due to thermal vibrations. Hence, the open-circuit current during the heating cycle decreases with time, as observed in Fig. 3(b). Similarly, in the cooling dT/dt < 0, the orientation of the dipoles is regained and spontaneous polarization increases. Thus, the current reversal is obtained as the free charges are again attracted to the surface. Fig. 3(c) shows the variation of temperature gradient and current with time for La-NBT-BT-Ta. Considering equation (3), I_p can be directly proportional to the dT/dt, which can also be observed in Fig. 3(c). Further, the dT/dt corresponding to the maximum current of 1.42 μA is 2.20 K/s.

The simulated temperature and current profiles are validated with Sharma et al. [15] work, as shown in Fig. 4. For this purpose, SBN is considered for the solar energy harvesting system because of the best performing material in their study. The results show that the present work accurately predicts the temperature (Fig. 4(a)) and current (Fig. 4(b)) under similar boundary conditions. Thus, it can be said that the present work results are in line with the literature.

Further, selecting the most appropriate pyroelectric material is challenging, considering the current profile. Thus, the voltage across different load capacitance (C_L) of 0.1 μF, 1 μF, 25 μF and 100 μF at 0.04 Hz frequency is measured for 300 s, presented in Fig. 5(a) and (b), (c) and (d), respectively. The voltage decreases with the increasing C_L from 1 μF to 100 μF. It is because the charge generated on the material's surface is constant for a given frequency, regardless of the load capacitance. As a result, charging a capacitor with a large C_L takes longer, resulting in a lower voltage at the end of 300 s. Further, it is observed that at 0.1 μF and 1 μF the voltage saturation takes place at 25 s and 150 s, respectively. However, with the increased C_L (25 μF and 100 μF), saturation is not attained till 300 s. This is due to low C_L where a small charge is needed; hence less time is required to saturate than high C_L. Additionally, the ripples produced in the voltage at low C_L are higher and decrease with the increase in capacitance. The voltage ripples are inversely proportional to the capacitance and frequency; thus, it is minimized at higher capacitance [38]. Fig. 5 shows that La-NBT-BT-Ta is the best pyroelectric material (giving a maximum output voltage of 35 V) at an optimum load capacitor of 1 μF. It is important to note that 0.1 μF and 1 μF load capacitors provided almost similar voltage output; however, the ripples in 0.1 μF are more, leading to higher power wastage, noise and distortions. La-NBT-BT-Ta is the best pyroelectric material for energy harvesting because of its higher pyroelectric coefficient at room temperature. The pyroelectric results are strongly affected by the La^{3+} and Ta^{5+} concentrations in the pure NBT-BT ceramics due to morphotropic phase boundary is shifted either to the BT-rich end (if La replaces Na and/or Bi and Ta replaces Ti) or the BT-poor end (if La replaces Na and/or Bi and Ta) (La replaces Ba and Ta replaces Ti) [51]. La-NBT-BT-Ta has the largest value of c/a ratio, which means that it

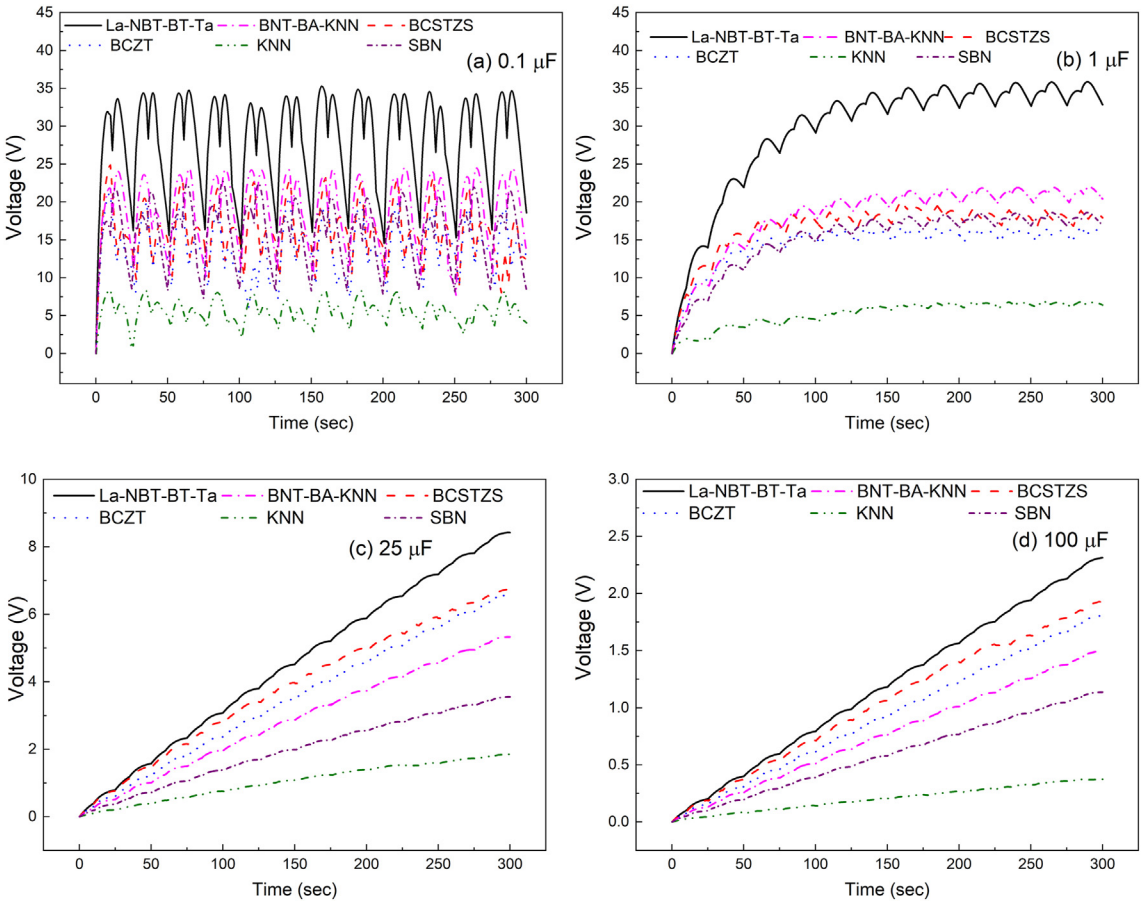

Fig. 5. Voltage as a function of time for (a) 0.1 μF, (b) 1 μF, (c) 25 μF and (d) 100 μF load capacitor at zero load resistance.

has a more tetragonal unit cell which contributes to an enhanced pyroelectric response. The La-NBT-BT-Ta have lower ε_r with higher p than the materials under consideration; thus, the pyroelectric FOMs increases. The simulated results are in good agreement with the experimental observation.

Thus, La-NBT-BT-Ta is further used to study the effect of different frequencies (0.5, 0.16, 0.08, 0.04, 0.02, 0.013 and 0.01 Hz) on the temperature and current output, as shown in Fig. 6. Fig. 6(a) and (b) show the temperature obtained for different heating/cooling cycle frequencies. The maximum temperature attained was inversely proportional to frequency; as heating time increases, the frequency decreases. The highest temperature attained was for the 0.01 Hz frequency as 327.5 K. Further, the corresponding current profiles for the same frequency are shown in Fig. 6(c) and (d). The maximum current during the heating cycle remains almost the same, ~1.42 μA for all the frequencies. However, the peak value of the current during the cooling cycle was obtained as 2.78 μA for 0.01 Hz frequency. The peak current value for the cooling cycle was increased with a decrease in frequency. It is because as frequency decreases, the cooling time also decreases. Hence, the temperature gradient for lower frequency increases during the cooling cycle, resulting in increased peak current, as seen in Fig. 6(d). The frequency analysis shows the maximum temperature and current obtained but does not provide the basis for choosing the working frequency for further studies.

In this regard, the output voltage at constant R_L (35 MΩ) and C_L (1 μF) under different frequencies is presented in Fig. 7(a) to obtain an optimum frequency value. The output voltage (V_o) increased with the increasing frequency till 0.04 Hz, then decreased. It is because voltage ripple decreases with an increase in frequency, which could be given as [52],

$$V_{ripple} = \frac{I_{dc}}{2 \times f \times C_L} \tag{10}$$

where V_{ripple} is the voltage ripple, I_{dc} is the rectified voltage, and f is the heating and cooling cycle frequency. Thus, the voltage ripple increases and the corresponding voltage across the R_L decreases if the frequency decreases. Hence, the frequency should be chosen in such a way that it maximizes voltage and power output. Thus, 0.04 Hz was suitable for low voltage ripple and expected to enhance power output. Moreover, finding the optimum R_L at which V_o would be maximum is essential. Fig. 7(b) shows the voltage at variation of R_L under 0.04 Hz and C_L (1 μF). It shows that with the increase in R_L output voltage (V_o) increases and beyond 55 MΩ (V_o = 18 V), the increment in voltage is not significant. Thus, it can be concluded that obtaining a maximal V_o, C_L of 1 μF, R_L of 55 MΩ and frequency of 0.04 Hz is required.

The above-discussed results are based on the FWR circuit; hence the validation of the simulation model of the FWR circuit is needed. Thus, the developed simulation model of FWR circuit is validated with the experimental work of Kumar et al. [53]. The experimental results are given for BCZT; hence, the same material is used to validate the simulation work. Fig. 8 (a) shows the open-source voltage of pyroelectric material when no circuit is connected. The results obtained from the simulation work agree with the experiments. However, there was a delay in the voltage phase as time increased. The experimental results cannot be perfectly sinusoidal

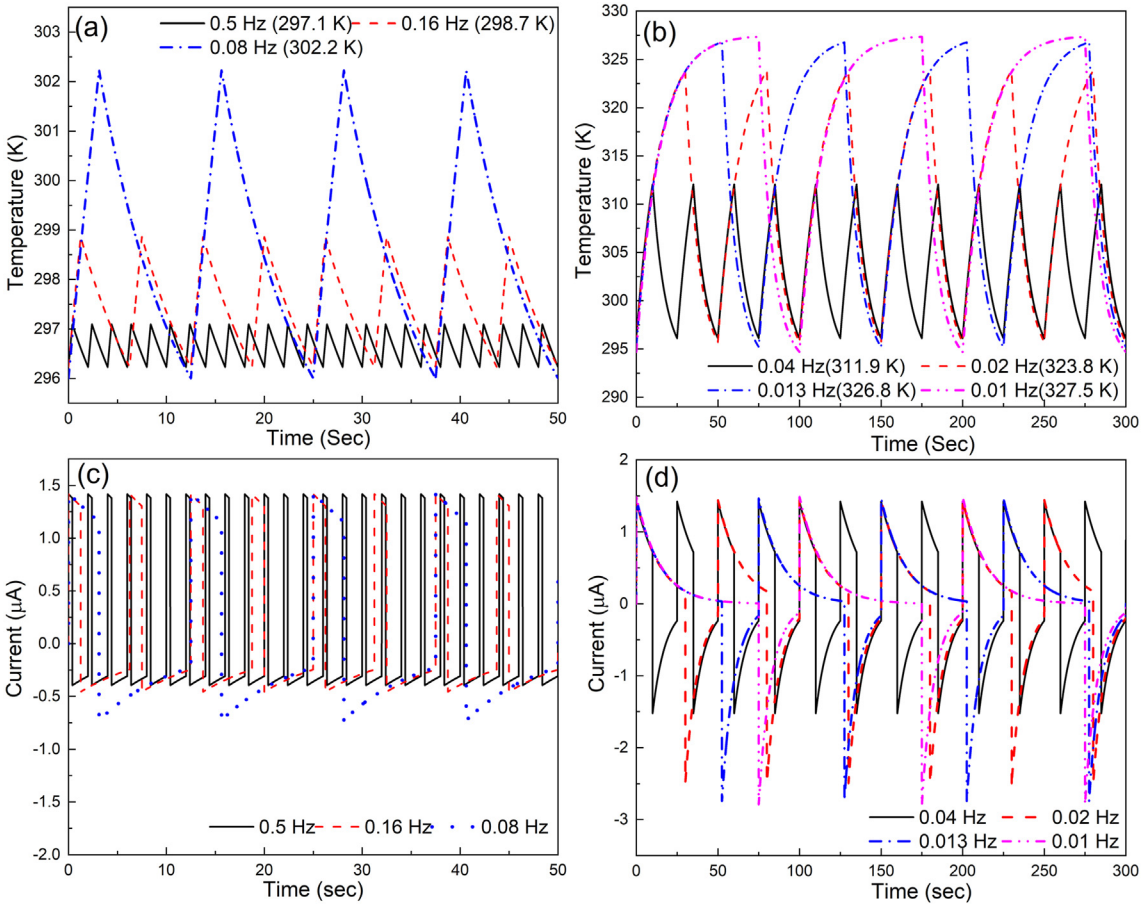

Fig. 6. Plot for La-NBT-BT-Ta temperature variation versus time and current versus time (a), (c) at high frequency (0.5, 0.16, 0.08 Hz) (b), (d) at low frequency (0.04, 0.02, 0.013, 0.01 Hz), respectively.

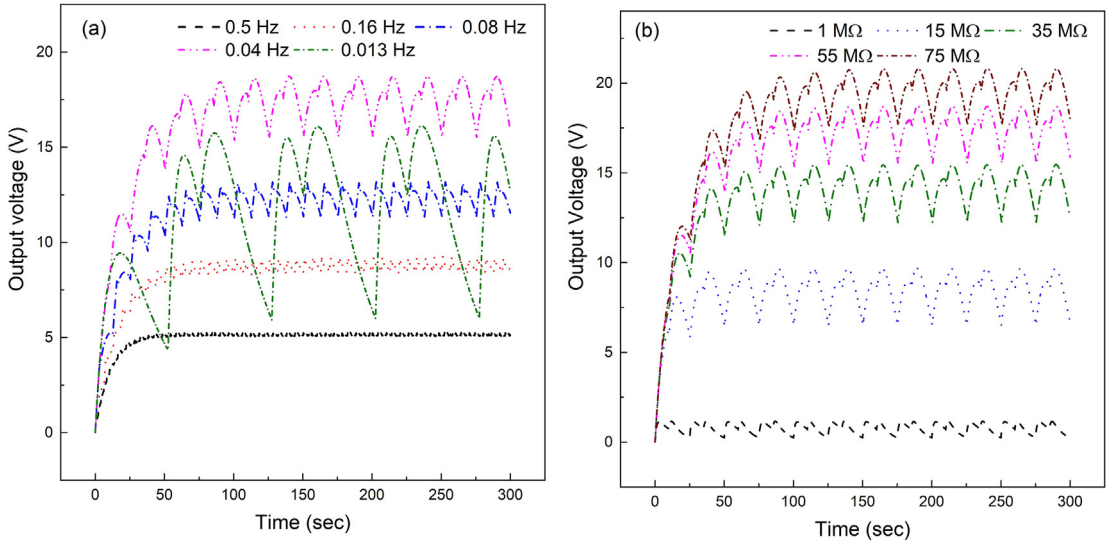

Fig. 7. Variation of output voltage for La-NBT-BT-Ta (a) at different frequencies under constant load resistance (R_L) of 35 MΩ and load capacitance (C_L) of 1 μF (b) at different R_L at a constant frequency of 0.04 Hz and C_L of 1 μF.

as there may be some delay during the heating and cooling cycle, which was not incorporated in the present model. Fig. 8(b) shows the power output at different values of load resistance. The power output also gives a good approximation in the R_L range of 5−20 MΩ. The maximum power output of 0.07 μW is obtained at R_L of 17−18 MΩ, similar to experimental work. Thus, it can be said that the simulation model can be used for the other pyroelectric materials' voltage and power analysis.

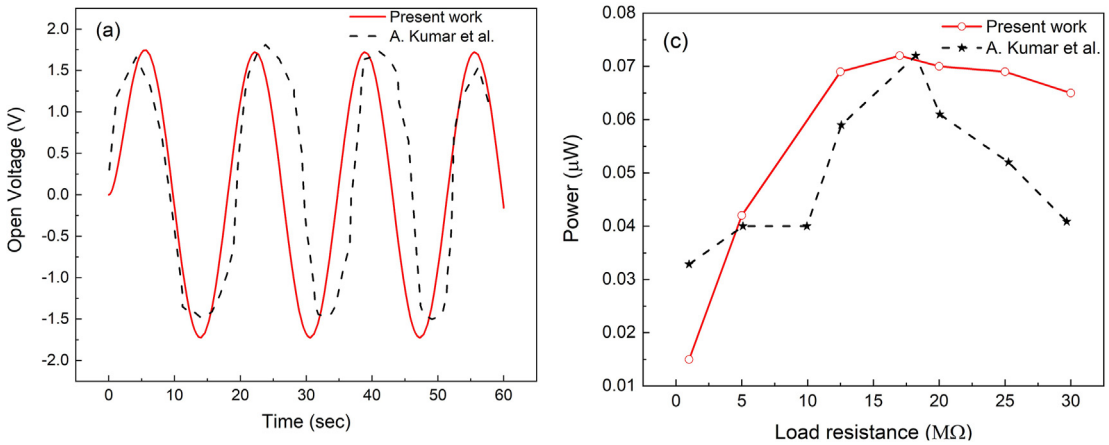

Fig. 8. Validation of FWR circuit simulation model for (a) open-circuit voltage versus time and (b) power output at different load resistance (R_L) with the experimental results of Kumar et al. [53].

The peak and mean power output for different R_L and constant C_L of 1 μF are shown in Fig. 9(a) and (b), respectively. The mean power was calculated to obtain the actual power available at the load resistance, considering the mean of the power ripple. The maximum peak power (6.7 μW) and mean power (5.3 μW) were obtained for 0.04 Hz, R_L of 25 MΩ and 35 MΩ, respectively. The peak power was obtained at R_L 25 MΩ, compared to the highest V_o at R_L 55 MΩ under 0.04 Hz and 1 μF. The shift of maximum power at low R_L is because; it is inversely proportional to resistance. Further, power varies with frequency due to its dependency on the V_o and R_L. The voltage ripples are high at a lower frequency, whereas low V_o is obtained at a higher frequency, leading to low power generation. Thus, the maximum peak and mean power output were obtained at 0.04 Hz.

Fig. 9 (c) shows the peak and mean power variation with frequency at a constant R_L of 55 MΩ. The peak and mean power output

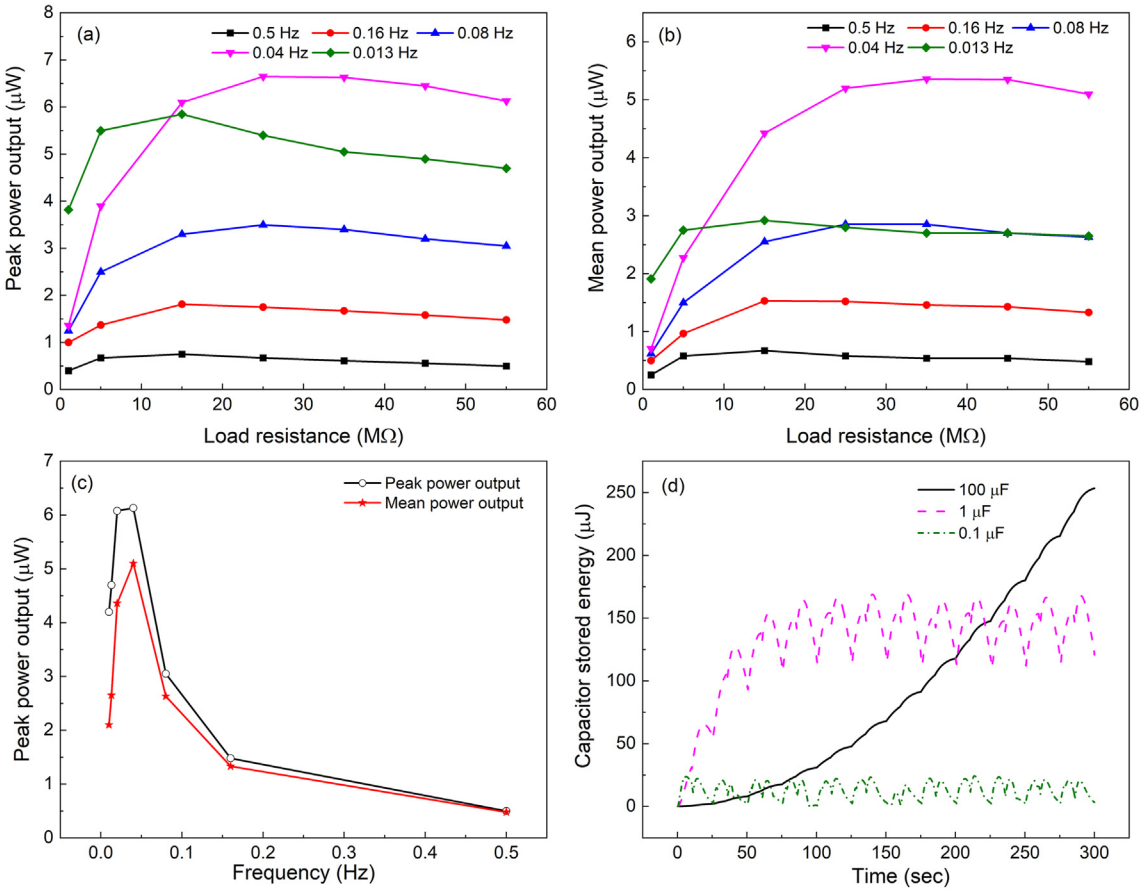

Fig. 9. (a) Peak power and (b) mean power for different load resistance and frequency, (c) Power output versus frequency at constant C_L of 1 μF and (d) Capacitor stored energy versus time at different C_L for La-NBT-BT-Ta.

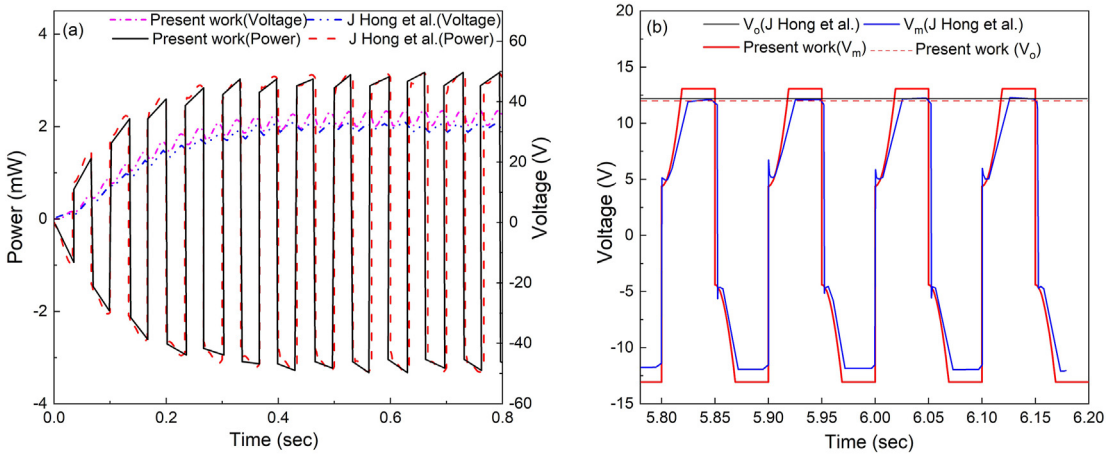

Fig. 10. Validation of the P−SSHI circuit (a) simulated power and voltage across the material capacitance (C_m) and (b) experimental voltage waveform (Hong et al. [54]) for V_m and V_o at C_m and C_L, respectively.

increase with frequency to a maximum of 6.17 μW and 5.06 μW, respectively, till 0.04 Hz and with further increase in frequency, power decreases. The solar energy harvested by pyroelectric material can also be stored in a small battery or capacitor for later use. If a capacitor is employed for energy storage (E), then it can be expressed by [13],

$$E = \frac{1}{2} C_L V_O^2 \tag{11}$$

The energy stored in the capacitors after 300 s for 0.1, 1 and 100 μF capacitance is shown in Fig. 9 (d). The maximum E of 250 μJ is obtained for the C_L of 100 μF. Though the maximum E is obtained for 100 μF, the open-circuit voltage (as seen in Fig. 5 (d)) and power output are low at the same capacitor. Thus, the most optimum C_L is in line with the results from the previous conclusions 1 μF as a comparable E of 175 μJ is obtained along with high V_o and power output.

In order to further enhance the power, P−SSHI and H−SSHI circuits are used. The P−SSHI circuit is validated with the literature and then employed for analysis. Thus, the results obtained from simulation for P−SSHI were verified with the theoretical and experimental work done by Hong et al. [54]. They have shown the voltage and power output for the piezoelectric materials considering higher frequency (15 Hz). The results were obtained using the present P−SSHI model and Hong et al. [54] are shown in Fig. 10(a) and (b) for similar input conditions and materials. It can be said that the present simulation model correctly validates the previous simulation and experimental work. However, ripples in the power output were present in this work due to voltage fluctuations. The P−SSHI circuit voltage V_m and V_o are obtained across C_m and C_L, validated with experimental work, as depicted in Fig. 10 (b). The maximum experimental V_m and V_o were obtained as 12 V and 12.2 V, and the simulated values were obtained as 11.9 and 13.2 V.

The P−SSHI circuit used for pyroelectric energy harvesting considers the frequency of 0.5 Hz. The peak power output from FWR, P−SSHI and H−SSHI employed at different R_L is shown in Fig. 11 at 0.5 Hz and 1 μF. The maximum peak power for FWR is found as 0.78 μW at 10 MΩ, whereas P−SSHI circuit shows ~54% improvement in peak power 1.2 μW (R_L = 15 MΩ). However, P−SSHI is required a power source to trigger the switch for the LC circuit, leading to the use of an auxiliary/external power supply. Thus, it is not easy to use due to precise time and consumes the energy generated from the materials to trigger the circuit. In this regard, a self-powered power circuit was required, which led to the consideration of H−SSHI. The H−SSHI used in this work is discussed in Fig. 2 and the power output is shown in Fig. 11. The maximum power of 1.05 μW is obtained at 15 MΩ, which is ~12.5% less than P−SSHI. However, this can be an effective technique because no external power source is required, and automatic triggering of the *LC* circuit can be done.

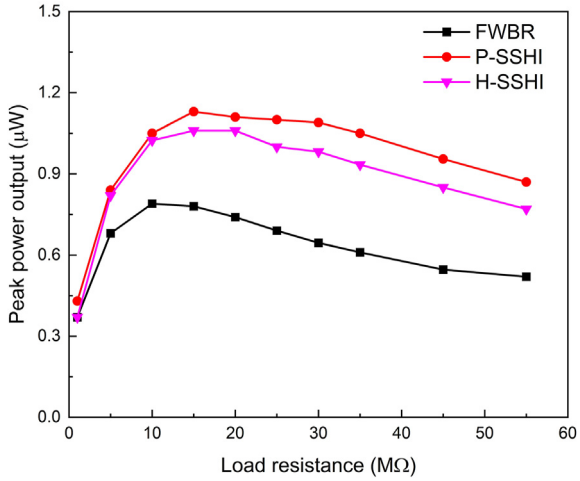

Fig. 11. Peak power output versus load resistance (R_L) at constant C_L of 1 μF and frequency of 0.5 Hz for different power-enhancing circuits.

However, from a frequency point of view, there are certain restrictions to using power-enhancing circuits for pyroelectric energy harvesting. The P−SSHI or H−SSHI circuits work well above 0.5 Hz only. It is because, below 0.5 Hz, the heating/cooling cycle time increases and current is obtained in a considerable period, making it difficult for SSHI to switch. Thus, SSHI circuits reduce the power output below 0.5 Hz at a low amplitude of temperature and current. Guyomar et al. [5] work also show that power output is affected by temperature amplitude, frequency of heating/cooling and volume of material. It suggests that a higher frequency and amplitude for maximum power output are needed for SSHI circuits. Thus, in the low-frequency region, a higher temperature amplitude is required for power-enhancing via SSHI. It makes the SSHI circuit practically challenging to use with solar heating-based energy harvesting. Hence, a further detailed investigation is required to ponder the use of low frequency for pyroelectric energy harvesting using SSHI circuits.

A number of other energy harvesting techniques are also available for the small devices. In this direction, the energy harvesting approach based on vibrations has been an active area of research; thus, Wei et al. [55] studied the three most prominent vibration-to-electricity conversion mechanisms: piezoelectric, electromagnetic and electrostatic [55]. The maximum power output of energy harvesters utilizing three distinct approaches ranges from 2.45×10^{-5} μW to 2.7×10^{4} μW. Electromagnetic energy harvesters perform a low-cost feature compared to piezoelectric energy harvesters. However, electromagnetic energy-collecting components often take up more space within the gadgets. The piezoelectric energy harvesters work with high-frequency ambient vibrations and a power output of up to 1.8 mW was attained [56]. Further, pyroelectric and piezoelectric show the 6.17 μW and 1.8 mW energy harvesting, respectively, where the power obtained from pyroelectric energy harvesting is low. However, from the practical application point of view, obtaining a frequency of 2580 Hz under environmental conditions is impossible [56], whereas pyroelectric energy harvesting for the present analysis under environmental conditions. Further, in this direction Tabbai et al. [57] presented the thermal phenomena occurring in a brake disc in use (heat flow produced by friction, strong thermal gradients, temperature rise, and the speed of rotation of the disc) were described. The maximum energy density harvested was 8.4 μJ cm^{-3}. Though a novel methodology is used for energy harvesting, the recovered voltage is limited by decreased pad thickness and increased speed [57]. The pad thickness and design would be a safety risk for its application in a real-time environment. The most widely used thermal harvesting method is thermoelectric generators (TEGs). TEGs are solid-state, non-moving-parts devices. However, thermoelectric generator is limited by the lower efficiency as in the case of pyroelectric energy harvesting. In a low-temperature regime, $\Delta T < 100$ °C, pyroelectric generators seem to have better power density than thermoelectric generators [58]. Photovoltaic (PV) technology is yet another intriguing and effective energy conversion method. The short wavelength photons of solar irradiance separate the electrons in the PV semiconductor, producing electrical current [59]. On the other hand, long-wavelength photons from the solar spectrum cannot excite electrons for separation and are instead converted to heat. The heat generated causes the temperature rise of the PV panel, which lowers the conversion efficiency. However, the efficiency of solar PV is much higher than pyroelectric energy harvesting but is restricted by heat generation [59]. In this direction, the solar photovoltaic may be embedded with pyroelectric materials to enhance energy harvesting. Thus, pyroelectric generators may not be an efficient technique for energy harvesting considering their peers but may be embedded with any other mechanism in a thermal gradient environment to enhance the power output.

5. Conclusions

The current study evaluates various lead-free pyroelectric materials for solar energy harvesting. Solar radiation was employed as a heat source, while natural airflow rate produced the necessary heating and cooling operations. La-NBT-BT-Ta is the most effective pyroelectric material providing a maximum voltage of 35 V at C_L of 1 μF under no-load conditions. The effect of frequency, load resistance, and capacitance were analyzed on La-NBT-BT-Ta to obtain maximum V_o (18 V at $R_L = 55$ MΩ) and power (6.17 μW at $R_L = 25$ MΩ) under 1 μF and 0.04 Hz frequency. The solar energy harvesting stored in a capacitor is obtained as 175 μJ for C_L of 1 μF. Nonlinear electrical circuits P–SSHI and H–SSHI enhanced the power by 54% and 42%, respectively, compared to FWR at 0.5 Hz. Thus, these approaches can potentially enhance the effectiveness of pyroelectric materials-based solar energy harvesting materials.

Data availability

All data generated or analyzed during this study are included within the article.

Declaration of competing interest

The authors declare that they have no known competing financial interests or personal relationships that could have appeared to influence the work reported in this paper.

Acknowledgments

S. Patel thanks the Science and Engineering Research Board for financial support in the frame of the Start-up Research Grant no. SRG/2020/000188.

References

[1] D. Ginley, M.A. Green, R. Collins, Solar energy conversion toward 1 terawatt, MRS Bull. 33 (2008) 355–364, https://doi.org/10.1557/mrs2008.71.
[2] L.L. Baranowski, G.J. Snyder, E.S. Toberer, Concentrated solar thermoelectric generators, Energy Environ. Sci. 5 (2012) 9055–9067. https://10.1039/c2ee22248e.
[3] H. Zhang, J. Baeyens, J. Degrève, G. Cacères, Concentrated solar power plants: review and design methodology, Renew. Sustain. Energy Rev. 22 (2013) 466–481, https://doi.org/10.1016/j.rser.2013.01.032.
[4] C.R. Bowen, J. Taylor, E. LeBoulbar, D. Zabek, A. Chauhan, R. Vaish, Pyroelectric materials and devices for energy harvesting applications, Energy Environ. Sci. 7 (2014) 3836–3856, https://doi.org/10.1039/C4EE01759E.
[5] D. Guyomar, G. Sebald, E. Lefeuvre, A. Khodayari, Toward heat energy harvesting using pyroelectric material, J. Intell. Mater. Syst. Struct. 20 (2009) 265–271, https://doi.org/10.1177/1045389X0809356.
[6] R. Whatmore, Pyroelectric devices and materials, Rep. Prog. Phys. 49 (1986) 1335, https://doi.org/10.1088/0034-4885/49/12/002.
[7] G. Sebald, E. Lefeuvre, D. Guyomar, Pyroelectric energy conversion: optimization principles, IEEE Trans. Ultrason. Ferroelectrics Freq. Control 55 (2008) 538–551, https://doi.org/10.1109/tuffc.2008.680.
[8] A.M. Balakt, C. Shaw, Q. Zhang, Large pyroelectric properties at reduced depolarization temperature in A-site nonstoichiometry composition of lead-free $0.94Na_xBi_yTiO_3$–$0.06Ba_zTiO_3$ ceramics, J. Mater. Sci. 52 (2017) 7382–7393, https://doi.org/10.1007/s10853-017-0973-1.
[9] N. Saurabh, S. Patel, Nonstoichiometric effect on electrocaloric, pyroelectric and energy storage properties of $0.94Na_xBi_yTiO_3$–$0.06BaTiO_3$ bulk ceramics, J. Mater. Sci. Mater. Electron. 32 (2021) 26871–26893, https://doi.org/10.1007/s10854-021-07063-2.
[10] S. Patel, A. Chauhan, R. Vaish, Large pyroelectric figure of merits for Sr-modified $Ba_{0.85}Ca_{0.15}Zr_{0.1}Ti_{0.9}O_3$ ceramics, Solid State Sci. 52 (2016) 10–18, https://doi.org/10.1016/j.solidstatesciences.2015.11.014.
[11] M. Sharma, V. Singh, S. Singh, P. Azad, B. Ilahi, N.A. Madhar, Porous $Ba_{0.85}Ca_{0.15}Zr_{0.1}Ti_{0.9}O_3$ ceramics for pyroelectric applications, J. Electron. Mater. 47 (2018) 4882–4891, https://doi.org/10.1007/s11664-018-6375-6.
[12] Z. Dai, D. Li, Z. Zhou, S. Zhou, W. Liu, J. Liu, X. Wang, X. Ren, A strategy for high performance of energy storage and transparency in KNN-based ferroelectric ceramics, Chem. Eng. J. 427 (2022), 131959, https://doi.org/10.1016/j.cej.2021.131959.
[13] C. Bowen, H. Kim, P. Weaver, S. Dunn, Piezoelectric and ferroelectric materials and structures for energy harvesting applications, Energy Environ. Sci. 7 (2014) 25–44, https://doi.org/10.1039/C3EE42454E.
[14] S. Patel, M. Kumar, Influence of grain size on the electrocaloric and pyroelectric properties in non-reducible $BaTiO_3$ ceramics, AIP Adv. 10 (2020), 085302, https://doi.org/10.1063/5.0017348.
[15] C. Bowen, J. Taylor, E. Le Boulbar, D. Zabek, V.Y. Topolov, A modified figure of merit for pyroelectric energy harvesting, Mater. Lett. 138 (2015) 243–246, https://doi.org/10.1016/j.matlet.2014.10.004.
[16] A.M. Balakt, C.P. Shaw, Q. Zhang, Giant pyroelectric properties in La and Ta co-doped lead-free $0.94Na_{0.5}Bi_{0.5}TiO_3$-$0.06BaTiO_3$ ceramics, J. Alloys Compd. 709 (2017) 82–91, https://doi.org/10.1016/j.jallcom.2017.03.143.
[17] X. Liu, D. Wu, Z. Chen, B. Fang, J. Ding, X. Zhao, H. Luo, Ferroelectric, dielectric and pyroelectric properties of Sr and Sn codoped BCZT lead free ceramics, Adv. Appl. Ceram. 114 (2015) 436–441, https://doi.org/10.1179/1743676115Y.0000000015.

[18] M. Sharma, A. Chauhan, R. Vaish, V.S. Chauhan, Finite element analysis on solar energy harvesting using ferroelectric polymer, Sol. Energy 115 (2015) 722–732, https://doi.org/10.1016/j.solener.2015.03.029.
[19] S.H. Krishnan, D. Ezhilarasi, G. Uma, M. Umapathy, Pyroelectric-based solar and wind energy harvesting system, IEEE Trans. Sustain. Energy 5 (2013) 73–81, https://doi.org/10.1109/TSTE.2013.2273980.
[20] C.-C. Hsiao, A.-S. Siao, Improving pyroelectric energy harvesting using a sandblast etching technique, Sensors 13 (2013) 12113–12131, https://doi.org/10.3390/s130912113.
[21] H. Nguyen, A. Navid, L. Pilon, Pyroelectric energy converter using co-polymer P (VDF-TrFE) and Olsen cycle for waste heat energy harvesting, Appl. Therm. Eng. 30 (2010) 2127–2137, https://doi.org/10.1016/j.applthermaleng.2010.05.022.
[22] J.H. Lee, K.Y. Lee, M.K. Gupta, T.Y. Kim, D.Y. Lee, J. Oh, C. Ryu, W.J. Yoo, C.Y. Kang, S.J. Yoon, Highly stretchable piezoelectric-pyroelectric hybrid nanogenerator, Adv. Mater. 26 (2014) 765–769, https://doi.org/10.1002/adma.201303570.
[23] J. Kim, S. Yamanaka, I. Murayama, T. Katou, T. Sakamoto, T. Kawasaki, T. Fukuda, T. Sekino, T. Nakayama, M. Takeda, Pyroelectric power generation from the waste heat of automotive exhaust gas, Sustain. Energy Fuels 4 (2020) 1143–1149, https://doi.org/10.1039/C9SE00283A.
[24] Y. Zhang, S. Kumar, F. Marken, M. Krasny, E. Roake, S. Eslava, S. Dunn, E. Da Como, C.R. Bowen, Pyro-electrolytic water splitting for hydrogen generation, Nano Energy 58 (2019) 183–191, https://doi.org/10.1016/j.nanoen.2019.01.030.
[25] D. Zabek, J. Taylor, V. Ayel, Y. Bertin, C. Romestant, C. Bowen, A novel pyroelectric generator utilising naturally driven temperature fluctuations from oscillating heat pipes for waste heat recovery and thermal energy harvesting, J. Appl. Phys. 120 (2016), 024505, https://doi.org/10.1063/1.4958338.
[26] M. Kang, E.M. Yeatman, Coupling of piezo-and pyro-electric effects in miniature thermal energy harvesters, Appl. Energy 262 (2020), 114496, https://doi.org/10.1016/j.apenergy.2020.114496.
[27] F.Y. Lee, A. Navid, L. Pilon, Pyroelectric waste heat energy harvesting using heat conduction, Appl. Therm. Eng. 37 (2012) 30–37, https://doi.org/10.1016/j.applthermaleng.2011.12.034.
[28] A. Cuadras, M. Gasulla, V. Ferrari, Thermal energy harvesting through pyroelectricity, Sens. Actuator A Phys. 158 (2010) 132–139, https://doi.org/10.1016/j.sna.2009.12.018.
[29] Q. Zhang, A. Agbossou, Z. Feng, M. Cosnier, Solar micro-energy harvesting with pyroelectric effect and wind flow, Sens. Actuator A Phys. 168 (2011) 335–342, https://doi.org/10.1016/j.sna.2011.04.045.
[30] M. Sharma, A. Chauhan, R. Vaish, V.S. Chauhan, Pyroelectric materials for solar energy harvesting: a comparative study, Smart Mater. Struct. 24 (2015), 105013, https://doi.org/10.1088/0964-1726/24/10/105013.
[31] I. Lien, Y. Shu, W. Wu, S. Shiu, H. Lin, Revisit of series-SSHI with comparisons to other interfacing circuits in piezoelectric energy harvesting, Smart Mater. Struct. 19 (2010), 125009, https://doi.org/10.1088/0964-1726/19/12/125009.
[32] J. Liang, W.-H. Liao, Energy flow in piezoelectric energy harvesting systems, Smart Mater. Struct. 20 (2010), 015005, https://doi.org/10.1088/0964-1726/20/1/015005.
[33] L. Wu, P. Zhu, M. Xie, A self-powered hybrid SSHI circuit with a wide operation range for piezoelectric energy harvesting, Sensors 21 (2021) 615, https://doi.org/10.3390/s21020615.
[34] P. Rakbamrung, M. Lallart, D. Guyomar, N. Muensit, C. Thanachayanont, C. Lucat, B. Guiffard, L. Petit, P. Sukwisut, Performance comparison of PZT and PMN–PT piezoceramics for vibration energy harvesting using standard or nonlinear approach, Sens. Actuator A Phys. 163 (2010) 493–500, https://doi.org/10.1016/j.sna.2010.08.028.
[35] H.S. Kim, J.-H. Kim, J. Kim, A review of piezoelectric energy harvesting based on vibration, Int. J. Precis. Eng. Manuf. 12 (2011) 1129–1141, https://doi.org/10.1007/s12541-011-0151-3.
[36] N. Sezer, M. Koç, A comprehensive review on the state-of-the-art of piezoelectric energy harvesting, Nano Energy 80 (2021), 105567, https://doi.org/10.1016/j.nanoen.2020.105567.
[37] H.A. Sodano, G. Park, D. Inman, Estimation of electric charge output for piezoelectric energy harvesting, Strain 40 (2004) 49–58, https://doi.org/10.1111/j.1475-1305.2004.00120.x.
[38] G. Sebald, D. Guyomar, A. Agbossou, On thermoelectric and pyroelectric energy harvesting, Smart Mater. Struct. 18 (2009), 125006, https://doi.org/10.1088/0964-1726/18/12/125006.
[39] V. Norkus, C. Plehnert, G. Hofmann, F. Nagel, C. Schiewe, Pyroelectric Multispectral Detectors and Their Applications, SPIE, 1994, pp. 87–96.
[40] G. Singh, V. Tiwari, P. Gupta, Electro-caloric effect in $(Ba_{1-x}Ca_x)(Zr_{0.05}Ti_{0.95})O_3$: a lead-free ferroelectric material, Appl. Phys. Lett. 103 (2013), 202903, https://doi.org/10.1063/1.4829635.
[41] S. Yao, W. Ren, H. Ji, X. Wu, P. Shi, D. Xue, X. Ren, Z.-G. Ye, High pyroelectricity in lead-free $0.5Ba(Zr_{0.2}Ti_{0.8})O_3$–$0.5(Ba_{0.7}Ca_{0.3})TiO_3$ ceramics, J. Phys. D . 45 (2012), 195301, https://doi.org/10.1088/0022-3727/45/19/195301.
[42] M. Shen, Y. Qin, Y. Zhang, M.A. Marwat, C. Zhang, W. Wang, M. Li, H. Zhang, G. Zhang, S. Jiang, Enhanced pyroelectric properties of lead-free BNT-BA-KNN ceramics for thermal energy harvesting, J. Am. Ceram. Soc. 102 (2019) 3990–3999, https://doi.org/10.1111/jace.16250.
[43] M. Chandrasekhar, P. Kumar, Synthesis and characterizations of BNT–BT–KNN ceramics for energy storage applications, Phase Transitions 89 (2016) 944–957, https://doi.org/10.1016/j.ceramint.2014.12.136.
[44] J. Yang, X. Hao, Electrocaloric effect and pyroelectric performance in (K, Na) NbO_3-based lead-free ceramics, J. Am. Ceram. Soc. 102 (2019) 6817–6826, https://doi.org/10.1111/jace.16598.
[45] M.A. Rafiq, M.E. Costa, A. Tkach, P.M. Vilarinho, Impedance analysis and conduction mechanisms of lead free potassium sodium niobate (KNN) single crystals and polycrystals: a comparison study, Cryst. Growth Des. 15 (2015) 1289–1294, https://doi.org/10.1021/cg5016884.
[46] A. Tsujii, T. Kasashima, M. Yamazaki, Y. Okimura, Application of (K, Na)NbO_3-based lead-free piezoelectric ceramics to ultrasonic sensors, J. Ceram. Soc. JAPAN. 128 (2020) 464–468, https://doi.org/10.2109/jcersj2.20009.
[47] J. Xie, X. Mane, C. Green, K. Mossi, K.K. Leang, Performance of thin piezoelectric materials for pyroelectric energy harvesting, J. Intell. Mater. Syst. Struct. 21 (2010) 243–249, https://doi.org/10.1177/1045389X09352818.
[48] R.L. Byer, C. Roundy, Pyroelectric coefficient direct measurement technique and application to a nsec response time detector, Ferroelectrics 3 (1972) 333–338, https://doi.org/10.1080/00150197208235326.
[49] A. Kumar, S. Kumar, S. Patel, M. Sharma, P. Azad, R. Vaish, R. Kumar, K. Srikanth, Pyroelectric energy conversion using $Ba_{0.85}Sr_{0.15}Zr_{0.1}Ti_{0.9}O_3$ ceramics and its cement-based composites, J. Intell. Mater. Syst. Struct. 30 (2019) 869–877, https://doi.org/10.1177/1045389X198284.
[50] V. Sidharthan, M.U. Bhasker, S. Korla, M. Chandrasekhar, Energy Harvesting of Synchronized Switch Harvesting on Inductor, IEEE, 2018, pp. 2882–2887, https://doi.org/10.1109/ICRIEECE44171.2018.9009273.
[51] A.M. Balakt, C.P. Shaw, Q. Zhang, Giant pyroelectric properties in La and Ta co-doped lead-free $0.94Na_{0.5}Bi_{0.5}TiO_3$-$0.06BaTiO_3$ ceramics, J. Alloys Compd. 709 (2017) 82–91, https://doi.org/10.1016/j.jallcom.2017.03.143.
[52] S. Gupta, N. Vamanan, V. John, A diode bridge rectifier with improved power quality using the capacitive network, IEEE Trans. Ind. Appl. 54 (2017) 1563–1572, https://doi.org/10.1109/TIA.2017.2785354.
[53] A. Kumar, R. Vaish, S. Kumar, V. Singh, M. Vaish, V. Singh Chauhan, K.S. Srikanth, Lead-free pyroelectric materials for thermal energy harvesting: a comparative study, Energy Technol. 6 (2018) 943–949, https://doi.org/10.1002/ente.201700819.
[54] J. Hong, F. Chen, M. He, S. Wang, W. Chen, M. Guan, Study of a low-power-consumption piezoelectric energy harvesting circuit based on synchronized switching technology, Energies 12 (2019) 3166, https://doi.org/10.3390/en12163166.
[55] C. Wei, X. Jing, A comprehensive review on vibration energy harvesting: modelling and realization, Renew. Sustain. Energy Rev. 74 (2017) 1–18, https://doi.org/10.1016/j.rser.2017.01.073.
[56] M. Ericka, D. Vasic, F. Costa, G. Poulin, S. Tliba, Energy Harvesting from Vibration Using a Piezoelectric Membrane, EDP sciences, 2005, pp. 187–193, https://doi.org/10.1051/jp4:2005128028.
[57] Y. Tabbai, A. Alaoui-Belghiti, R. El Moznine, F. Belhora, A. Hajjaji, A. El Ballouti, Friction and wear performance of disc brake pads and pyroelectric energy harvesting, Int. J. Precis. Eng. Manuf.- Greeen tech. 8 (2021) 487–500, https://doi.org/10.1007/s40684-020-00195-6.
[58] R.A. Kishore, S. Priya, A review on low-grade thermal energy harvesting: materials, methods and devices, Materials 11 (2018) 1433, https://doi.org/10.3390/ma11081433.
[59] A. Mohammadnia, A. Rezania, B.M. Ziapour, F. Sedaghati, L. Rosendahl, Hybrid energy harvesting system to maximize power generation from solar energy, Energy Convers. Manag. 205 (2020), 112352, https://doi.org/10.1016/j.enconman.2019.112352.